

# Mechanism of quiescent nanoplastic formation from semicrystalline polymers

Received: 30 October 2024

Accepted: 14 March 2025

Published online: 28 March 2025

 Check for updates

Nicholas F. Mendez<sup>1</sup>, Vivek Sharma<sup>2</sup>, Michele Valsecchi<sup>1</sup>, Vighnesh Pai<sup>1</sup>, Johnny K. Lee<sup>1</sup>, Linda S. Schadler<sup>3</sup>, Alejandro J. Müller<sup>4,5</sup>, Shelby Watson-Sanders<sup>6</sup>, Mark Dadmun<sup>6</sup>, Guruswamy Kumaraswamy<sup>2</sup>✉ & Sanat K. Kumar<sup>1</sup>✉

Polymers are known to spontaneously produce microplastics (sizes 1  $\mu\text{m}$  – 3 mm) and nanoplastics (10 nm – 1  $\mu\text{m}$ ). Still, the mechanisms by which environmentally-triggered Å-level random bond breaking events lead to the formation of these relatively large fragments are unclear. Significantly,  $\approx 70\%$  of commercial polymers are semicrystalline, with a morphology comprised of alternating crystalline and amorphous layers, each tens of nanometers thick. It is well-accepted that chain scission events accumulate in the amorphous phase. We show that this leads to mechanical failure and the concurrent release of particulate nanoplastics comprised of polydisperse stacks of lamellae even under quiescent conditions. Noncrystalline analogs, which do not have a well-defined microstructure, do not form nanoplastics. While the amorphous phase of the semicrystalline nanoplastics continues to degrade, crystal fragments do not, and hence, they temporally persist in the environment. These results stress the critical role of polymer microstructure and fracture mechanics on particulate nanoplastic creation.

The world's plastic production continues to increase, and with recycling rates lagging, plastic waste continues to accumulate<sup>1</sup>. Approximately 75% of all plastic used is either landfilled or cast into the environment<sup>2</sup>, leading to fragmentation into smaller objects, i.e., microplastics (MPL, sizes between 1  $\mu\text{m}$  and 5 mm)<sup>3–5</sup> and nanoplastics (NPL, sizes between 10 nm and 1  $\mu\text{m}$ )<sup>6–11</sup>. These particles' temporal persistence and size allow them to penetrate cell membranes and accumulate within organisms, potentially harming aquatic life<sup>12</sup>, plants<sup>13,14</sup>, and humans<sup>15–18</sup>. For example, their presence in heart plaque has been correlated with heart disease, stroke, and death<sup>19</sup>.

Polymers in the environment are subject to a host of degradation cues, such as hydrolysis, oxidation, ultraviolet irradiation, and mechanical stresses<sup>7,20,21</sup>, which lead to bond cleavage<sup>22</sup>. Literature reports clearly illustrate that such bond-breaking events

are necessary for MPL and NPL formation, but previous authors have variously proposed that the underpinning mechanisms could be chemi-crystallization, void-formation, cracking, and/or embrittlement<sup>23–25</sup>. Thus, there is no detailed, molecular-level understanding of how local Å-scale bond-breaking events lead to fragment formation. Enunciating these mechanisms, focusing specifically on NPL formation under quiescent conditions, is the emphasis of this work.

Approximately 70% of consumer plastics are semicrystalline and have a lamellar morphology<sup>26</sup>. This structure is characterized by alternating crystalline lamellae and amorphous regions, each tens of nanometers thick, which are hierarchically assembled into larger-scale superstructures, e.g., spherulites<sup>27,28</sup>. It is established that the environmental degradation of semicrystalline

<sup>1</sup>Department of Chemical Engineering, Columbia University, New York, New York 10027, USA. <sup>2</sup>Department of Chemical Engineering, Indian Institute of Technology Bombay, Mumbai 400076, India. <sup>3</sup>Department of Mechanical Engineering, University of Vermont, Burlington, VT 05405, USA. <sup>4</sup>POLYMAT and Department of Advanced Polymers and Materials: Physics, Chemistry and Technology, Faculty of Chemistry, University of the Basque Country UPV/EHU, Paseo Manuel de Lardizabal 3, 20018 Donostia-San Sebastián, Spain. <sup>5</sup>IKERBASQUE, Basque Foundation for Science, Plaza Euskadi 5, Bilbao 48009, Spain. <sup>6</sup>Department of Chemistry, University of Tennessee Knoxville, Knoxville, TN 37996, USA. ✉e-mail: [guruswamy@iitb.ac.in](mailto:guruswamy@iitb.ac.in); [sk2794@columbia.edu](mailto:sk2794@columbia.edu)

polymers<sup>29–31</sup> primarily occurs in the amorphous regions<sup>32,33</sup>, since solvents/gases do not readily penetrate the amorphous phase. We propose that, as degradation progresses, the accumulation of bond-breaking events in the amorphous phase ultimately leads to the mechanical failure of the material. Under these conditions, we observe the fragmentation of the hierarchical morphology into NPL comprised of single or multiple crystals and any associated undegraded amorphous phase (Fig. 1A). While the latter continues to degrade, the temporal persistence of the crystalline domains results in their environmental accumulation. Here, we validate this correlation between degradation-driven failure and fragmentation that leads to NPL creation.

## Results

### Role of polymer morphology in NPL formation

While most previous work has focused on the changes to bulk polymers undergoing degradation<sup>23–25,34,35</sup>, here we also critically analyze

the material released into the surroundings. We study commercial grades of polypropylene (PP), poly(ethylene terephthalate) (PET), and polystyrene (PS), which are respectively the second, fourth, and fifth most produced polymers worldwide. Parenthetically, while commercial samples typically have stabilizing additives, samples with no additives have speeded-up degradation but with no qualitative changes to NPL creation mechanisms (Supplementary Fig. 1). We consider both amorphous and semicrystalline PP samples [respectively, atactic (aPP) and isotactic (iPP,  $\approx 63\%$  crystallinity)]; films with thickness  $\approx 100\ \mu\text{m}$  and PS [respectively, atactic (aPS) and syndiotactic (sPS,  $\approx 79\%$  crystallinity), film thickness  $\approx 100\ \mu\text{m}$ ] to investigate the role of microstructure on degradation mechanisms (see Table 1 for polymer information). We note that the amorphous phase of the PP sample is rubbery under the conditions investigated, while the PS is glassy. We show that this does not cause any qualitative changes in the observed behavior. These samples are oxidatively degraded in aqueous potassium persulfate ( $\text{K}_2\text{S}_2\text{O}_8$ ) solutions at  $70\ ^\circ\text{C}$  (see Methods,

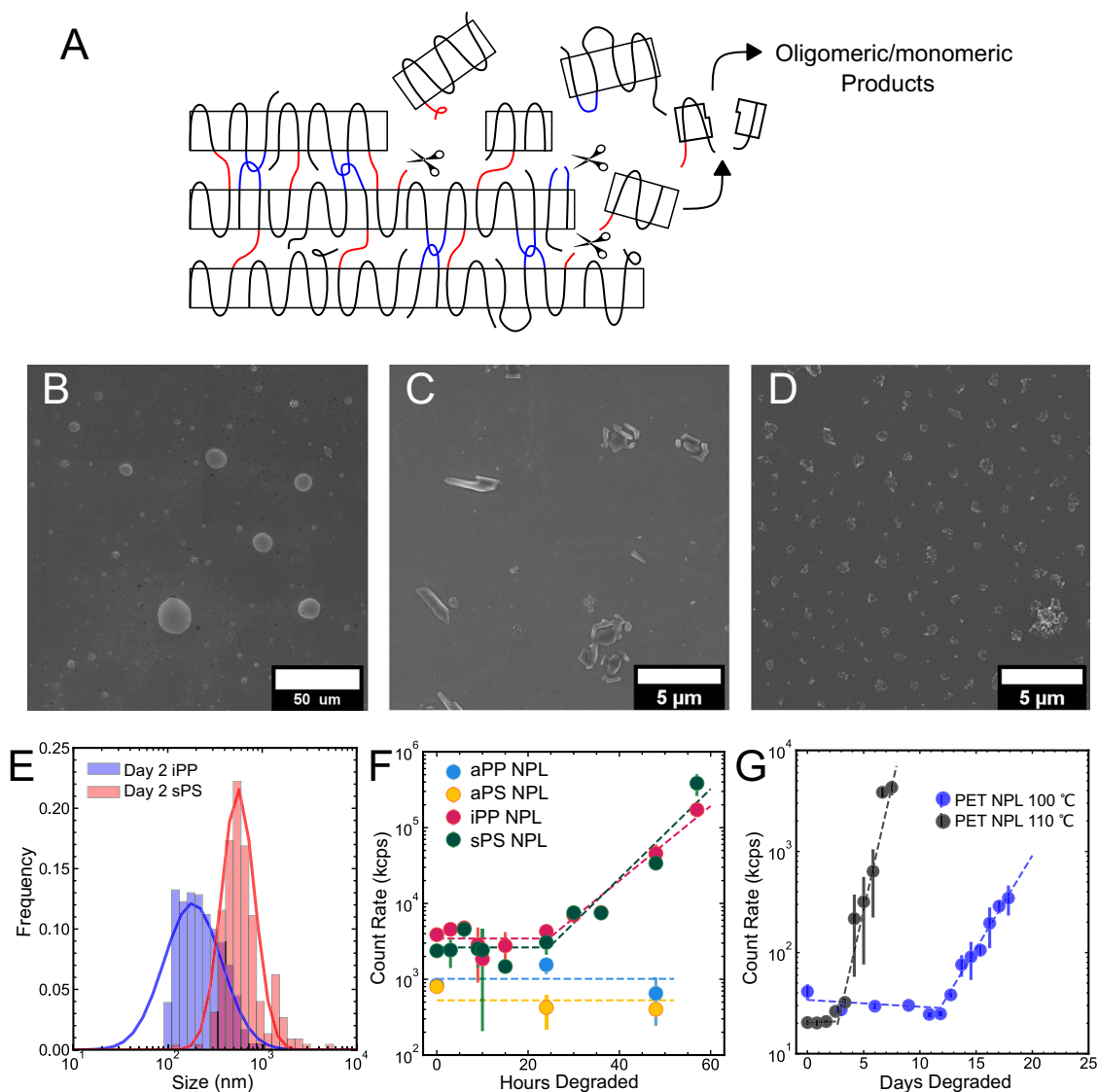


**Fig. 1 | Impact of Polymer Morphology on NPL Formation.** **A** Schematic illustration of chain scission in the amorphous regions of a semicrystalline polymer (red represents bridges, blue represents bridging entanglements). **B–D** SEM micrographs of solution samples obtained after 2 days of degradation of **B** aPP, **C** sPS and **D** iPP films in aqueous  $\text{K}_2\text{S}_2\text{O}_8$  at  $70\ ^\circ\text{C}$ . While the iPP and sPS samples clearly contain NPL, aPP appears to produce only liquid-like droplets which we postulate to be comprised of oligomeric degradation products that phase separate

during solvent evaporation. **E** Size distributions of iPP and sPS NPL obtained after 2 days of degradation from SEM micrographs. The curves are guides to the eye. **F, G** Light scattering count rate as a function of time at an angle of  $175^\circ$  for **F** the oxidative degradation of iPP, aPP, sPS and aPS (dashed lines for aPP and aPS are averages of the scattering counts after 48 h of degradation) and for **G** the hydrolysis of PET. Error bars shown are the standard deviation of the mean.

**Table 1 | Summary of polymers used. Melting Temperature ( $T_m$ ) measured by differential scanning calorimetry (DSC) for all samples and glass transition temperature ( $T_g$ ) measured by DSC for PET**

Polymer	Supplier	$T_g$ (°C)	$T_m$ (°C)	$M_w$ (kDa)
PET (hydrolysis)	Goodfellow	78	245	28 <sup>70</sup>
PET (glycolysis)	Post consumer Coca-Cola bottles	78	245	52
iPP	Reliance Industries	-5 <sup>71</sup>	161	399
aPP	Sigma-Aldrich	-5 <sup>71</sup>	-	30
sPS	Idemitsu Kosan	100 <sup>72</sup>	247	178
aPS	Supreme Petrochem (India)	100 <sup>72</sup>	-	274

Molecular weight for iPP, aPP, sPS, and aPS measured by rheology (Supplementary Note 2, Supplementary Fig. 3).

Supplementary Note 1 and Supplementary Fig. 2). In addition, we also degrade PET films (thickness  $\approx 250$   $\mu\text{m}$ , 27% crystallinity) by hydrolysis<sup>35–39</sup> in ultra-pure water at 100 °C and 110 °C, and by glycolysis at 180 °C. (Amorphous PET samples could not be studied due to cold crystallization under degradation conditions). Preliminary investigations for a polar polymer, Nylon 6, degraded by 2 M HCl also yielded similar results.

Due to the slow polymer degradation kinetics under ambient conditions, we employ accelerated degradation conditions that allow for NPL creation in reasonable timeframes. Using accelerated aging tests has a long, venerable, and well-tested history in the polymer field<sup>23,24,29,35,40</sup>, and data at different temperatures are typically merged into a master curve. Regardless, the mechanisms employed are analogous to environmental degradation<sup>40,41</sup>. PET hydrolysis is a known environmental degradation pathway<sup>42</sup> and has been shown to occur over long timescales at ambient conditions. By raising the temperature, we simply accelerate it<sup>35</sup>. Glycolysis of PET is not a natural pathway<sup>43–45</sup>, but mechanistically it follows hydrolysis in that it results in ester cleavage. While UV and heat act over the whole sample, persulfate oxidation of the PP and PS primarily occurs near the surface (see below). However, they both serve as free radical initiators for chain fragmentation<sup>40,41</sup>, and persulfate oxidation is significantly faster than UV/heat induced NPL creation.

We experimentally characterize the presence of NPL in solution and estimate their size distribution by combining scanning electron microscopy (SEM) and light scattering (LS). Light scattering intensity convolves the NPL concentration, size and shape. We find that data at a scattering angle of 175°, and data at 15° yield qualitatively similar trends. Electron microscopy results show that the NPL sizes are highly polydisperse and that their shapes also vary considerably (and generally are far from spherical). So, it is not possible to unambiguously determine the NPL size and concentration from the scattering intensity. Thus, we use the net scattering intensity as a proxy that convolves all of these factors. Specifically, a lack of scattering implies little to no NPL in solution. After two days of oxidative degradation, the solutions containing aPP and aPS films show minimal scattering. SEM on the dried aPP and aPS solutions show the existence of large ( $\approx 10$   $\mu\text{m}$ ) spherical droplets, likely formed by phase separation of oligomeric degradation products during solvent evaporation (Fig. 1B, Supplementary Fig. 4). In contrast, the sPS (Fig. 1C) and iPP (Fig. 1D) samples release a significant number of polydisperse, asymmetric objects ranging from tens of nm to  $\approx 10$   $\mu\text{m}$  into the solution (Fig. 1E), which we identify as particulate MPL and NPL (Supplementary Figs. 5–6; Supplementary Table 1). The particles have a platelet-like shape with large lateral dimensions. The NPL formed by PET are comparable to those shown in Fig. 1C and D (Supplementary Fig. 7), but we note that this data may be affected by terephthalic acid (TPA) crystals which form

during PET hydrolysis; PET glycolysis suffers from no such issue as we shall discuss below. We generally find that the size ranges of the NPL are similar across the iPP, sPS, and PET systems, and fragmented plastics appear to span from nanometers to microns in size (Fig. 1E). The SEM results are consistent with light scattering intensity measurements: aPP (835 kcps) and aPS (800 kcps) scatter substantially less than iPP and sPS (52000 kcps for iPP and 33000 kcps for sPS) solutions after 2 days of degradation.

### Mechanism of NPL formation

We now focus on the NPL formation processes – in particular, we demonstrate the existence of an induction time prior to significant NPL release. Specifically, the light scattering intensity increases for iPP and sPS after  $\approx 25$  h (Fig. 1F), while for PET it increases after  $\approx 3$  days for 110 °C and  $\approx 12$  days for 100 °C (Fig. 1G). Note that the degradation of PET essentially occurs homogeneously across the film<sup>23</sup>, whereas the degradation of PP and PS is largely limited to the film surface<sup>40,46–48</sup>. Known diffusion coefficients imply that water will permeate through a  $\approx 250$   $\mu\text{m}$  thick PET film in about 1 h at 110 °C, leading to an equilibrium water sorption of  $\approx 1\%$  by weight<sup>49,50</sup>, which is nearly two orders of magnitude shorter than the NPL induction time at that temperature. On the other hand, the high reactivity of the OH radical created by the hydrolysis of the potassium salt used in iPP and sPS degradation makes it unlikely that the bulk regions are significantly affected in the earlier stages of degradation.

These differences in transport/degradation mechanisms manifest themselves as different temporal evolutions of the mechanical properties of PET and iPP samples, as measured using a tensile tester (stress/strain curves are presented in Supplementary Figs. 8–10). The maximum stress measured in PET samples hydrolyzed at 110 °C (Fig. 2A) does not change significantly during the first day of degradation, after which it rapidly decreases to a lower plateau at 3 days. Meanwhile, Young's modulus of PET at 110 °C (Fig. 2B) is approximately time-independent. These results are consistent with those observed by Arhant et al. and demonstrate that PET loses toughness after a critical amount of time which follows an Arrhenius dependence on temperature (with an activation energy  $E_a \approx 120$ –130 kJ/mol)<sup>23</sup>. Importantly, this kink in maximum stress at 3 days has previously been shown to coincide with the time where the essential work of fracture, from double notched fracture tests, goes to zero<sup>51</sup>. Our results show that the loss in mechanical integrity, as quantified by the essential work of fracture going to zero, correlates with the release of PET NPL (Fig. 1G) since both phenomena show an induction time of  $\approx 3$  days at 110 °C. Similar results are found for PET degraded at 100 °C as both the induction time for NPL release (Fig. 1G) and loss of mechanical integrity (shown in Supplementary Fig. 10) occur at  $\approx 12$  days.

In contrast to these findings for homogeneously degraded PET samples, the mechanical properties of the surface-degraded iPP show very different temporal evolution (the sPS samples were too brittle to perform tensile tests). We degrade thin ( $\approx 3$   $\mu\text{m}$  thickness) films by persulfate oxidation and measure their mechanical response as a function of degradation time. We used thinner samples here to amplify the effects of surface oxidative attack. The Young's modulus and the maximum stress that these samples can support are initially approximately constant but suddenly drop after  $\approx 25$  h (Fig. 2C and D), which corresponds to the induction time for NPL release (Fig. 1F). Thicker samples ( $\approx 100$   $\mu\text{m}$ ) show the same onset time for this decrease, but the magnitude of decrease is smaller. These results are surprising since Young's modulus is thought to be directly related to crystallinity<sup>52</sup>, which remains constant (or increases slightly after degradation). Instead, we propose that this result is caused by failure of the sample surface due to extensive cracking (Fig. 2E and F) – in these situations, since a smaller proportion of the film's cross-section carries load during a tensile test, there is an apparent decrease in Young's modulus (which is calculated using the original sample thickness). This is

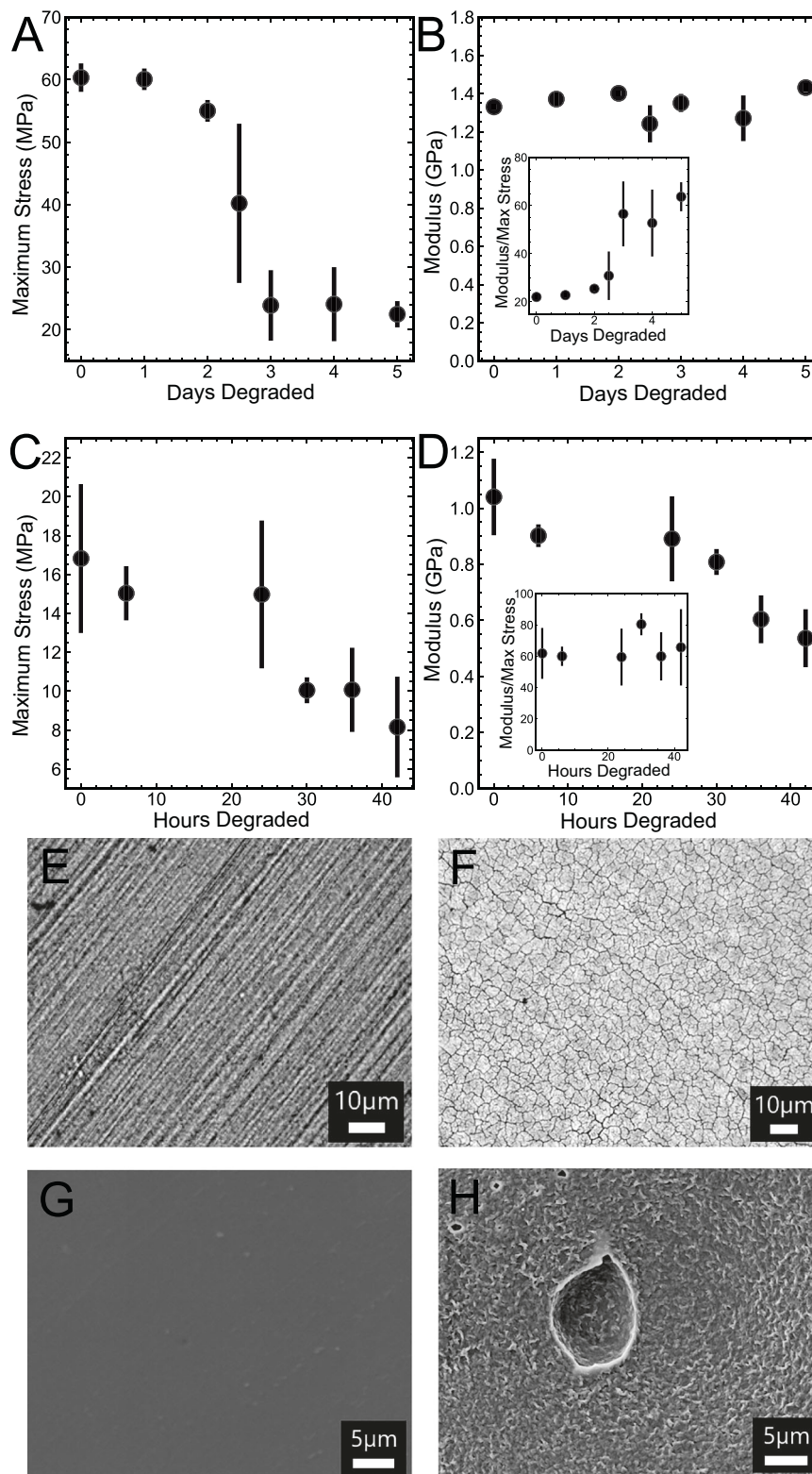


**Fig. 2 | Mechanical Properties of Degraded Polymer Films.** **A, B** Degradation time-dependent mechanical properties, from tensile testing, for the hydrolytic degradation of PET at 110 °C. **A** maximum stress, **B** modulus, inset shows the ratio of modulus to maximum stress. **C, D** Corresponding data for the oxidative degradation of iPP. **C** maximum stress, **D** modulus, inset shows the ratio of

modulus to maximum stress. Error bars shown in **A–D** are the standard deviation of the mean. **E, F** Optical microscope images of the surface of iPP films after degradation for 0 and 96 h, respectively. **G, H** SEM images of the surface of PET films after degradation for 0 and 14 days, respectively.

supported by the concurrent drop observed in the maximum stress at failure. We note that the ratio of Young's modulus to failure stress remains approximately constant (Fig. 2D, inset), suggesting that, as expected, surface cracks affect both Young's modulus and maximum stress similarly. Comparatively, the surface of the hydrolyzed PET films shows only weathering with the formation of pits (Fig. 2G and H).

Our key conclusion is that the loss of mechanical integrity of semicrystalline materials (i.e., their inability to support stress) correlates with the release of NPL, although the specifics of this result are sensitive to whether the whole film or the surface degrades. However, both cases lead to the same qualitative behavior, with NPL released from the surface after a critical induction time that is also accompanied by a significant worsening of the material's mechanical properties.

We now turn to the physics underpinning this failure. Since the relevant materials are semicrystalline, we invoke the well-established idea that bridges and bridging entanglements (collectively known as tie-molecules) that connect adjacent crystals are critical to their mechanical integrity<sup>53–56</sup>. While it is accepted that the scission of enough of these connectors leads to material failure, there is considerable controversy about the details of this process<sup>57,58</sup>. Here, we postulate that the induction time can be related to a surface energy per unit area that in this case corresponds to the energy required to cut enough tie-molecules for a fragment to release. Thus, we develop these ideas qualitatively to provide a physical picture: quantitatively accurate predictions require a predictive theory, which currently does not exist.

In the amorphous phase of a semicrystalline polymer, there are three kinds of chain fragments: bridges, loops, and tails (Fig. 1A). Loops can be entangled with other loops belonging to the opposing crystal lamella to form bridging entanglements which act as stress transmitters akin to bridges. The temporal evolution of the number  $n_k$  of each chain fragment type follows:  $\frac{d \log n_k}{d \log(1-\phi)} = \bar{l}_k$  (see Supplementary Note 3). Here,  $\phi$  is the fraction of total reactive backbone bonds that have degraded in the amorphous regions at a given time, while  $\bar{l}_k$  is the (instantaneous) average number of reactive bonds in chains fragments of type  $k$ . The key physics here is that the mean length of tie-molecules is significantly longer than that of unentangled loops and tails. As a means of illustrating this point, the classic Gambler's Ruin model<sup>59</sup>, which is known to be approximate but qualitatively correct, predicts that the average number of bonds in loops and bridges scale as  $l_a$  and  $l_a^2$ , respectively, where  $l_a$  is the amorphous phase thickness. According to this simplified picture, the PET samples studied here should possess  $\approx 20$  cleavable bonds per bridge, while the iPP samples have  $\approx 100$  cleavable bonds per bridge; these differences are caused by the variation in  $l_a$  and persistence length between the two polymers. Let us define  $\phi_{B,0.5}$  as the critical degraded bond fraction needed to cause the scission of 50% of the bridges. Since  $\frac{n_B}{n_{B,0}} \approx (1-\phi)^{l_{B,0}} \approx e^{-\phi l_{B,0}}$ , for the PET sample, we estimate  $\phi_{B,0.5}^{\text{PET}} \approx 0.04$  while for the iPP sample  $\phi_{B,0.5}^{\text{iPP}} \approx 0.01$ . Since bridging entanglements (intended here as the pair of entangled loops) are approximately twice as long as bridges, the corresponding degradation fractions  $\phi_{BE,0.5}$  will be half as big as those estimated for bridges. The key point here, of course, is that enough tie-molecules are broken, and thus the sample is unable to transmit stress between opposing lamellae when only a relatively small fraction of amorphous phase bonds are broken. Thus, NPL formation occurs early in the degradation process, and the NPL produced will have a significant fraction of the amorphous phase in addition to the crystalline domains. Below, we show that these amorphous chain fragments also degrade away with time, leaving only lamellar crystals as a long-lived environmental pollutant.

### NPL Structure and Properties

Characterizing NPL properties is challenging as their mass is  $\approx 1\%$  or less of the starting film mass, as measured by weighing the films before

and after degradation. Thus, many of our measurements are signal-to-noise limited. Nevertheless, we employ DSC, polarized light optical microscopy (PLOM), attenuated total reflection Fourier transform infrared spectroscopy (ATR-FTIR), thermogravimetric analysis (TGA), and small/wide angle x-ray scattering (SAXS/WAXS) to gain structural/chemical insights into NPL properties. This characterization provides strong evidence that NPL have similar properties to the corresponding bulk material. We focus on a few essential results here and defer most of this characterization to the Supplementary Information.

When PET degrades, it produces ethylene glycol (water soluble) and TPA (water insoluble and crystallizes). The samples were centrifuged and dried to accumulate mass for the experiments, but this protocol ensured that only the water-insoluble products remain. Characterization of the starting PET films and pure TPA is presented in the Supplementary Figs. 11–18. In Fig. 3A we present DSC data – specifically, the second heating of a bulk PET and two PET NPL samples where the heat flow is normalized by the PET sample mass (i.e., excluding the TPA mass). The first melting behavior of the PET NPL shows large sample-to-sample variations, likely due to the size and shape polydispersity of the NPL created, but upon subsequent cooling followed by heating, all the NPL melt in a similar temperature range as the bulk PET (full DSC trace shown in Supplementary Figs. 19–20). This confirms the presence of crystallizable PET in the NPL samples. The crystallinity of the samples from the second heating is 24% for the bulk, while the NPL samples show crystallinities of 63% and 55% for samples obtained after 14 and 28 days of degradation, respectively. The increase in crystallinity for the NPL samples, relative to the bulk, likely comes from chain scission in the NPL, resulting in higher achievable crystallinity upon recrystallization. These DSC results are complemented by TGA (Fig. 3B) and ATR-FTIR (Fig. 3C). The ATR-FTIR data shows that the peak corresponding to the carbonyl functional group at  $1716 \text{ cm}^{-1}$  typical of bulk PET is present in all NPL samples; however, as degradation progresses, a new peak forms at  $1675 \text{ cm}^{-1}$  corresponding to the free carboxylic acid end groups of TPA – full spectra are presented in the Supplementary Fig. 21 (spectra for PP and PS systems presented in Supplementary Figs. 22–23). TGA measurements highlight two events at  $\approx 300 \text{ }^\circ\text{C}$  and  $\approx 400 \text{ }^\circ\text{C}$ , which correspond to TPA sublimation and PET degradation, respectively (pure PET and TPA degradation shown in Supplementary Fig. 24). TGA analysis shows that the PET NPL present in solution after 7 days of degradation are composed of  $\approx 81 \pm 3\%$  PET (and hence  $\approx 19\%$  TPA), while this number falls to  $\approx 53 \pm 1\%$  and  $\approx 24 \pm 3\%$  PET for the samples degraded for 14 days and 28 days, respectively.

PLOM measurements with  $90^\circ$  cross-polarizers were used to observe the melting behavior of the PET NPL by using the DSC melting protocol on a hot stage. The results show that the PET NPL drop-cast from solution are birefringent, as expected for a semicrystalline morphology (Fig. 3D). Birefringence is lost beyond  $230 \text{ }^\circ\text{C}$ , while complete melting occurs at  $300 \text{ }^\circ\text{C}$  (Fig. 3E), consistent with the DSC melting temperature of the bulk material. Upon cooling, the NPLs recrystallize from the melt into their semicrystalline spherulitic state, which displays the expected Maltese cross-extinction patterns, Fig. 3F (further temperature intervals are in Supplementary Fig. 25). The sPS NPL show similar melting and recrystallization behavior (Fig. 3G–I). iPP results are shown in Supplementary Fig. 26. SAXS and WAXS results discussed in the Supplementary Note 4–6 and Supplementary Figs. 27–35) show that the long period of the PET decreases with degradation time in the bulk films, while the lamellar thickness remains approximately constant, at least within the uncertainties in these estimates. This is consistent with the notion that degradation preferentially occurs in the amorphous regions of the semicrystalline morphology. These results are similar to observations in the photodegradation of low-density polyethylene<sup>60</sup> and the radiation ageing of polyoxymethylene<sup>61</sup>. We note that the PET NPL long period is smaller than that of the corresponding bulk, while the crystal thickness is slightly smaller.

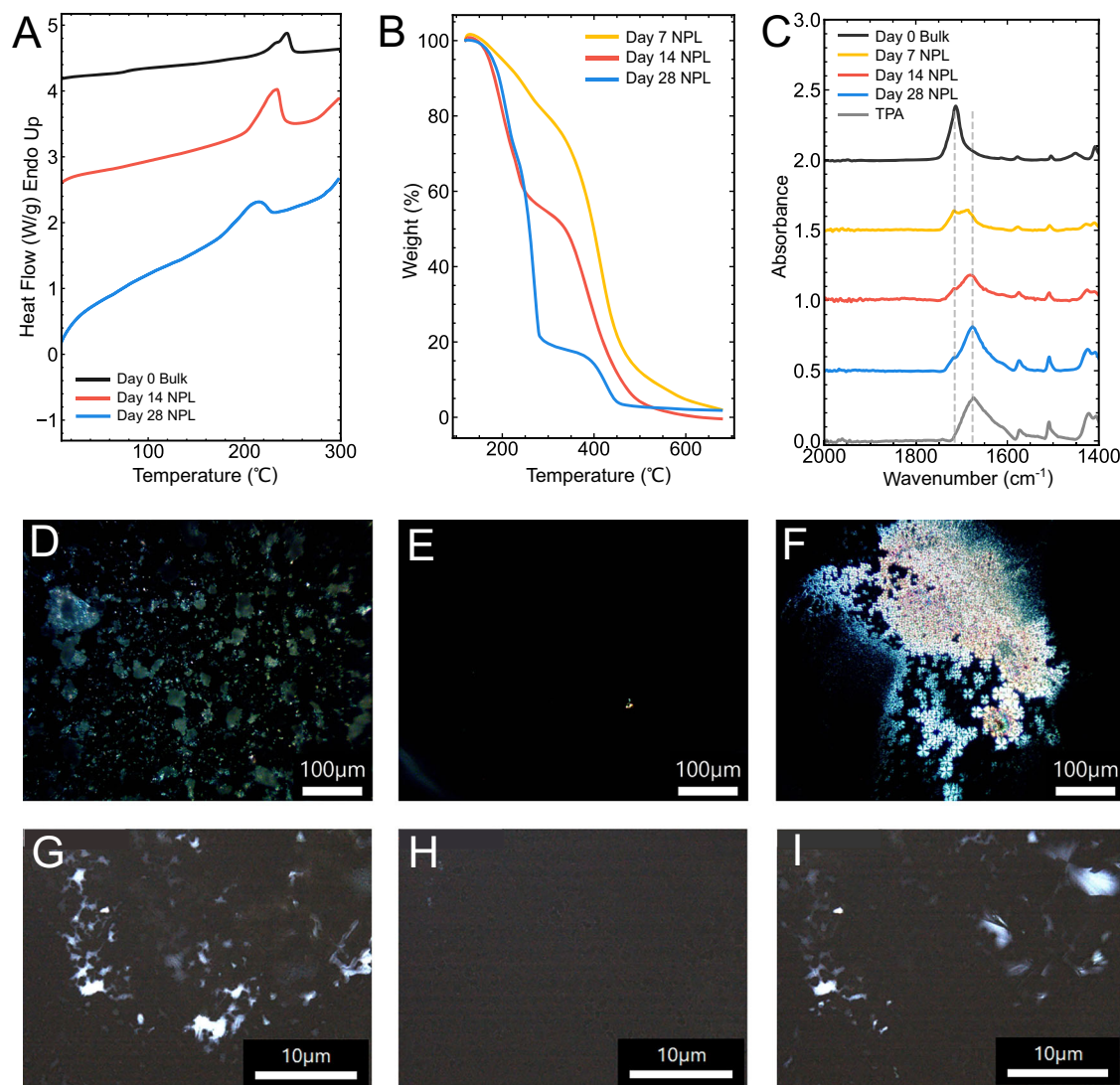


**Fig. 3 | Characterization of NPL Samples.** **A** Second DSC heating scans of PET NPL conducted at a ramp rate of 10 °C/min; curves are shifted vertically for clarity and the data is normalized to the heat flow of PET (using TGA to determine PET content). **B** TGA of PET NPL at a ramp rate of 30 °C/min under nitrogen. **C** ATR-FTIR spectra of PET NPL compared to a semicrystalline bulk sample and TPA. Dashed

lines indicate the carbonyl peak of bulk PET and TPA, respectively; curves are shifted vertically for clarity. **D–F** PLOM images of PET NPL taken at **D** room temperature prior to heating, **E** 300 °C (melted), and **F** 100 °C (recrystallized). **G, H** PLOM images of sPS NPL taken at **G** 100 °C (prior to melting), **H** 235 °C (melted), and **I** 100 °C (recrystallized).

### Continued Degradation of NPL

To examine the aging behavior of NPL particles without the bulk material present, we further degrade the sPS, iPP, and PET NPL after removing the films from the solution (see Methods). The sample notation is indicated as ‘Day X + Y’ where ‘X’ refers to the degradation time with the films in solution (to generate the initial NPL) and ‘Y’ refers to the time for additional degradation of the NPL after the films are removed from solution. Figure 4A and B show that at the beginning of this experiment, the PET sample is composed of  $\approx 81 \pm 3\%$  PET, while the additional 12-day-aged sample is composed of  $\approx 20 \pm 6\%$  PET (the remaining is TPA; errors are from 3 measurements). No significant additional degradation is seen in the 19-day aged sample. Presumably, the amorphous phase of the PET degrades away in the first 12 days of aging, while the crystals do not significantly degrade even after 7 days of further aging.

To further support the notion that the crystal persists upon quiescent degradation of semicrystalline polymers, we present results of PET glycolysis at 180 °C. This protocol has several advantages. First, as noted above, glycolysis causes ester cleavage as in hydrolysis, but a

key difference is that the monomer produced in glycolysis, [Bis(2-Hydroxyethyl) terephthalate], is soluble in ethylene glycol. In addition, glycolysis allows us to totally fragment the material in time scales of hours, which provides us with an answer to what remains after long degradation times. Thus, after 75 min of glycolysis, the film falls apart and forms a white, highly crystalline PET powder ( $\approx 90\%$  crystallinity) that is insoluble in ethylene glycol. The nature of this crystalline product is discussed in detail in reference<sup>62</sup> but here we focus on a key result. Transmission electron microscopy (TEM) shows a representative NPL produced after the glycolysis reaction and the corresponding electron diffraction image, Fig. 4C and D. It is clear that this representative object is nearly 0.5  $\mu\text{m}$  in lateral size, but that it is a single crystal, as seen by the sharp electron diffraction spots observed. While some particles are observed to be polycrystalline (shown in Supplementary Fig. 36), the survival of single crystals under extreme degradation conditions, where essentially no amorphous material remains, shows the temporal stability of the polymer crystal.

In the same vein, the NPL from the sPS and iPP samples show a clear decrease in average size with continued degradation in the

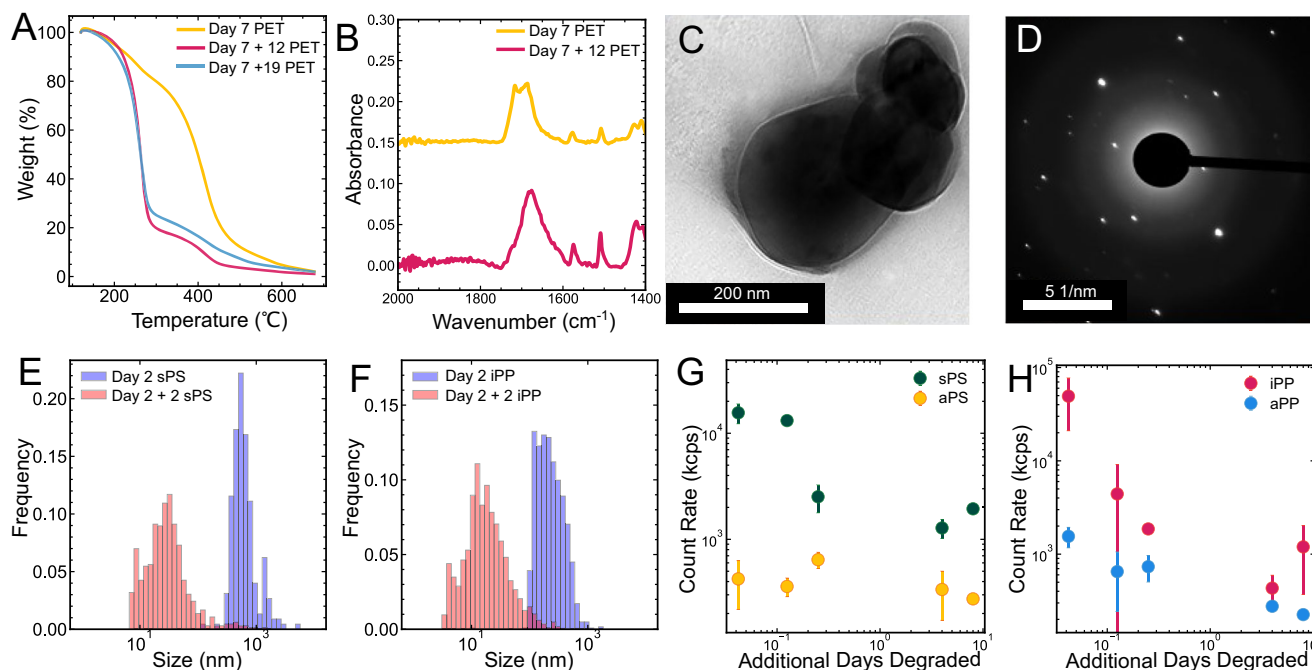


**Fig. 4 | Continued Degradation of NPL Particles.** **A** TGA scans of a PET NPL sample obtained after 7 days of film hydrolysis at 110 °C. After film removal we aged the samples for a further 12 and 19 days, respectively. The TGA experiments were conducted under nitrogen at a ramp rate of 30 °C/min. **B** ATR-FTIR of the carbonyl region for two of the three PET samples in **A**. **C** Image and **D** corresponding electron diffraction of PET NPL remaining after complete glycolysis of PET bottles.

**E, F** Size distributions from SEM of NPL after 2 days of degradation (with the bulk film present, blue), and the same sample solution after 2 additional days of degradation with no bulk sample present (red) for **E** sPS and **F** iPP. **G, H** Count rate measurements from light scattering after bulk films are removed from solutions and NPL continue to degrade for **G** sPS and aPS and **H** iPP and aPP. Error bars shown are the standard deviation of the mean.

absence of the films, with the large particles disappearing (Fig. 4E, F), and the smallest fragments being  $\approx 10$  nm in size. Light scattering measurements for continued degradation experiments on PP and PS (Fig. 4G, H) demonstrate that the stereoregular polymers always display higher scattering intensities than their amorphous counterparts. Together, these results reinforce the notion that the crystalline domains persist under quiescent conditions and that polymer microstructure has a key role in NPL formation.

## Discussion

Taken together, our results show that NPL have unique structural properties, highlighting that they are very different from commercial NPs, such as PS nanospheres. Such commercial nanomaterials are inadequate if we want to delineate the role of NPL in toxicity studies<sup>63</sup>.

We propose that NPL can fragment all the way down to individual lamellae. Separately, they can also fragment laterally into smaller objects. The work of Kolmogorov<sup>64</sup> shows that the lateral fragment sizes should eventually follow a log-normal distribution. The trends we observe for the largest lateral size of the fragments obtained from iPP and sPS oxidation are consistent with this model (Figs. 1E, 4E, and F). Therefore, successive fragmentation events can explain the observed size distribution of NPL. Note that the size distributions measured in the current work are similar to those found for nanocrystals obtained through acidic degradation of cellulose<sup>65</sup>.

Of course, real-life aging would not be under quiescent conditions, other than perhaps for landfilled plastics – rather, other factors, such as wind and wave action and abrasion, will accelerate these processes. In these cases, by analogy, the material should fracture when the external stress exceeds the failure strength of these materials. Additionally, our preliminary work suggests that external stress can only fragment polymers down to a size scale of  $\approx 100$ –200 nm – smaller particles are unaffected by these outside forces, and then the quiescent ideas presented here become relevant. Regardless, the NPL

created, especially their crystalline elements, are expected to have a substantial environmental lifetime.

Finally, our results indicate a potentially fruitful approach to reduce or prevent NPL formation: strengthening the amorphous phase by increasing the number of bridges and entangled loops while decreasing their length could result in lower NPL creation rates<sup>66</sup>.

## Methods

### Materials

A summary of polymer sources is presented in Table 1. Pure terephthalic acid (TPA) was purchased from Sigma Aldrich. Potassium persulfate ( $K_2S_2O_8$ ) and potassium hydroxide were obtained from Merck. 1,5,7-Triazabicyclo[4.4.0]dec-5-ene, Methanesulfonic Acid, and Ethylene glycol were sourced from Fischer Scientific. Distilled, deionized water from a Millipore Milli-Q system is used for oxidation experiments. Hydrolysis reactions use HPLC Plus water purchased from Sigma Aldrich. The reaction vessels are 75 mL round bottom pressure vessels with a polytetrafluoroethylene (PTFE) lid from ChemGlass. These pressure vessels are necessary since the hydrolysis reactions occur at temperatures above water's normal boiling point.

### Reaction procedures

**Hydrolysis.** The initially amorphous PET films ( $\approx 250$   $\mu$ m thickness) were crystallized from the glassy state (cold crystallization) by heating them from room temperature to 120 °C for 30 min (Supplementary Figs. 37–38). This initial step enables the starting material to be semicrystalline with a crystallinity of 27% as measured by DSC (note that even performing the cold crystallization at 150 °C yielded the same starting crystallinity within the typical uncertainty of the measurements, i.e. approximately 10%). After recrystallization, the films are weighed and cut into rectangles before being washed with HPLC water to remove surface dust and any fragmented material resulting from cutting. The cut films are then sealed in the reaction vessels with HPLC

water at 100 mg/mL concentration. Vessels are heated in an oil bath to 110 °C (or 100 °C) for varying lengths of time. After removal from the oil bath, the solution is filtered into glass containers using a 1 mm wire mesh. At the same time, the film is dried in an oven under vacuum at 60 °C (below the glass transition temperature,  $T_g$ ) for 12 hours. The solution containing NPL is then used either as is or dried to a powder (after centrifugation). Additionally, the NPL solution is placed in a clean pressure vessel for continued degradation. Steps conducted in open air are performed in a laminar flow hood to limit dust contamination. Water blanks are run in parallel with reaction experiments to monitor any trace contaminants. These blanks yielded predominantly dust on the micron scale, allowing us to distinguish objects in microscopy samples.

**Oxidation.** As received pellets of the iPP, aPP, sPS, and aPS are washed with isopropyl alcohol (IPA) before melt-pressing. The IPA used is filtered using a PVDF filter of pore size 0.22  $\mu\text{m}$ . PP and PS samples are sandwiched between PTFE sheets (thickness  $\approx$  1 mm) and pressed under the hot plates (temperature maintained at 250 °C and 320 °C, respectively) at a pressure of 2 bar for 1 min using a TSI Hot Polymer press. The films ( $\approx$  100  $\mu\text{m}$  thickness for NPL experiments,  $\approx$  30  $\mu\text{m}$  thickness for mechanical property measurements) are allowed to cool to ambient temperature, and the pressure is released to obtain the film. Before degradation experiments, the films are washed thrice with filtered MilliQ water and dried under dry nitrogen using an air gun.

Degradation of PP and PS samples was performed using oxidation methods previously described in the literature<sup>40</sup>. Briefly,  $\approx$  10 g of melt-pressed PP and PS films are taken in triplicates in 100 ml of MilliQ water in borosilicate Pyrex bottles. Each sample is heated to 70 °C to achieve the optimal activation efficiency of  $\text{K}_2\text{S}_2\text{O}_8$ . Then, 4 grams of  $\text{K}_2\text{S}_2\text{O}_8$  are added. A 0.4 g/mL aqueous KOH solution is then added at intervals of 6 h to keep the pH of the solution at  $\approx$  7.00. The KOH neutralizes the  $\text{H}_2\text{SO}_4$  generated by the decomposition of  $\text{K}_2\text{S}_2\text{O}_8$  (see Supplementary Information Note 1). Over 2 days, 2.195 mL of KOH solution is added in total to the reaction mixture. After 2 days, the polymer films are removed from the bottle to allow for the continued degradation of NPL. 40  $\mu\text{l}$  of the KOH solution are added to 2 mL of the residual dispersion to increase the pH so that the remaining NPL continues to be subjected to oxidative degradation.

**Glycolysis.** The catalyst was prepared using the same methods created by Jehanno et al.<sup>67</sup>. The salt catalyst was prepared by mixing Triazabicyclodecene (TBD) and Methanesulfonic acid (MSA) at molar ratios of acid to base of 1:1 at 80 °C for 20 min or until solidified. The product obtained was a transparent and homogenous solid<sup>67</sup>. Ethylene Glycol (EG), TBD: MSA catalyst, PET (20:0.5:1 molar ratio), and stir bar were all placed in a 20 mL reaction vial inside a glovebox, sealed with septa, and transferred outside the glovebox into a 180 °C oil bath. Previous studies indicate that this reaction takes under 2 h at 180 °C to reach completion<sup>67</sup>. After the reaction was allowed to run for a set time, the reaction vials were taken from the oil bath. The ethylene glycol (EG) and depolymerization products soluble in EG were immediately decanted hot from the reaction vials. The remaining solid PET that is insoluble in EG was washed with water three times by suspending it in 20 mL of water and stirring with a stir bar for 15 min. After the third wash and decant, the reaction vial containing the EG insoluble materials was set on a 70 °C hotplate overnight to evaporate any remaining water.

### Instruments and characterization

**DSC.** Thermal properties are measured using a TA Instruments Discovery 250 DSC. The instrument is calibrated using sapphire disks for heat capacity and indium for temperature and enthalpy. The sample chamber is purged with nitrogen. The experimental protocol uses a heat-cool-heat cycle, which ramps at 10 °C/min from 10 °C to 300 °C

followed by cooling at the same rate down to 10 °C followed by another heating at the same rate to 300 °C. PET crystallinity values are calculated by dividing the 1<sup>st</sup> heating cycle enthalpy of melting by the melting enthalpy of a fully crystalline PET (140.1 J/g)<sup>68,69</sup>. Note that some works use different melting enthalpy values, which may lead to slight differences compared with our work<sup>23,51</sup>.

**Tensile testing.** The mechanical properties of PET samples are tested using a Chatillon CS2 testing machine with a 500 N load cell. The samples' films are cut into dogbone geometries using an ISO 527 type 5A die. Samples are tested at a speed of 1 mm/min until failure. The data presented are averaged over at least 5 replicates for each sample. Strain is calculated from the instrument displacement over the gauge length of the samples. Stress is calculated using the pre-deformed cross-sectional area. The mechanical properties of iPP samples are tested on a Linkam MFS tensile stage equipped with a load cell of 200 N and at a crosshead speed of 0.5 mm/min until failure. The samples' films are cut into rectangular strips with dimensions 30 mm  $\times$  2 mm  $\times$  30  $\mu\text{m}$ . The tensile measurements are averaged for at least 5 replicates, and samples that failed near the grips were not included in the averaging.

**PLOM.** PLOM of PET samples is performed using an AmScope microscope with 90° crossed polarizers and an MP 14 digital camera operating in reflection mode. A Linkam HFSX350V-CAP temperature hot stage is used for in situ temperature control. Samples are drop-cast and dried on silicon wafers prior to melting. The samples are then heated from ambient temperature to 300 °C at a ramp rate of 10 °C/min and cooled at the same rate. Image analysis is conducted using the AmScope software.

For the PP and PS samples, PLOM is performed on an Olympus BX53M microscope with 90° crossed polarizers and a FLIR Grasshopper-3 3.2 MP camera operated in transmission mode. A Linkam MFS, equipped with a hot stage, is used for in situ temperature-controlled optical microscopy. 5  $\mu\text{l}$  of the solution are drop-cast on piranha-cleaned glass slides used for imaging. Since the solution consists of the unreacted  $\text{K}_2\text{S}_2\text{O}_8$ ,  $\text{K}_2\text{SO}_4$ , and KOH, along with the generated NPL, it is important to separate the NPL from the salts for imaging. The drop is left to dry slowly (5  $\mu\text{l}$  in 48 h) by keeping it in a humid environment. As the water evaporates, the dispersed plastic fragments are deposited near the drying front as the contact line recedes due to the so-called coffee-ring effect. The dissolved salt moves with the shrinking water droplet and eventually precipitates to form a deposit at the centre of the drying drop. This results in spatial separation between the plastic fragments and the salt, which aids the imaging experiments.

**ATR-FTIR.** FTIR spectroscopy on PET samples is performed with a Fischer Scientific Nicolet iS20 spectrometer equipped with a diamond crystal smart iTX accessory to perform ATR. 16 scans are performed per run with a resolution of 0.482  $\text{cm}^{-1}$ . Background measurements are conducted between each sample, and the data is analyzed using the OMNIC software. For the PS and PP samples, FTIR spectroscopy is performed using a Bruker Alpha II spectrometer equipped with a diamond crystal to perform ATR. 24 scans per run are performed with a resolution of 4.0  $\text{cm}^{-1}$ . For each sample, background scans are run, and the data is analyzed using the SpectraGryph tool.

**SEM.** SEM imaging of PET NPL is performed both on samples that are drop-cast onto silicon wafers and on the dried powder deposited on carbon tape. PET films are imaged by mounting films on copper tape. In all cases, the samples are blown with air to remove loose material and sputter coated with Au/Pd (80/20) using a Safematic CCU-010 to coat the samples with a 5 nm conductive layer. Imaging is performed on a Zeiss Sigma VP. Images are taken at an accelerating voltage of 5 kV and analyzed in ImageJ.

For the PS and PP samples, SEM and energy dispersive x-ray spectroscopy (EDS) are performed using a ZEISS Ultra-55 Scanning Electron Microscope at an accelerating voltage of 5 kV. 5  $\mu$ l of the solution are collected at different time intervals and drop-cast on a silicon wafer. They are then slow-dried using the protocol used for PLOM. EDS is employed to confirm that the structures imaged are plastic fragments rather than salt crystals.

The ImageJ software is used to extract the particle size distribution from SEM micrographs. The raw data is imported to ImageJ, and an auto-threshold protocol is used (Supplementary Fig. 39). We verify the auto-thresholding process by comparing the pixel histogram against the greyscale values. The threshold obtained from the auto-threshold tool aligns with the threshold at the highest pixel count (Supplementary Fig. 39D). The 3D Object counter tool is used to determine the size distribution of MPL/NPL particles. To check the robustness of the thresholding protocol, the threshold is varied by  $\pm 5\%$ . We observe no qualitative variation in the particle size distribution obtained, suggesting that the protocol is robust to the choice of threshold (Supplementary Fig. 39C).

**TGA.** Thermal degradation and concentration measurements for PET samples are conducted using a TA Instruments TGA 550. The experimental procedure first involves ramping to 120  $^{\circ}$ C, followed by an isothermal hold for 30 min to fully remove water. After drying, the samples are heated at 30  $^{\circ}$ C/min to 700  $^{\circ}$ C to completely degrade the material.

**Light scattering.** Light scattering measurements on PET samples are taken using a Malvern Zetasizer Nano ZS and disposable poly(methyl methacrylate) cuvettes. The detector scattering angle is 175 $^{\circ}$ , and the temperature is controlled at 25  $^{\circ}$ C. Samples of the reaction solution are tested at regular intervals to measure the increase in count rate over time without employing any attenuation protocol. The presented data are all averages of 3 individual measurements.

For the PS and PP samples, time-dependent sample fragmentation is measured using light scattering experiments on a Lightsizer 500 DLS (Anton Paar). Measurements are done in triplicates at a scattering angle of 175 $^{\circ}$  with temperature controlled at 25  $^{\circ}$ C in a quartz cuvette for 10 seconds. We obtain the unattenuated scattering intensity, expressed as kilocounts/second, at varying degradation times. While particle sizes can be obtained from a cumulant fit to the time correlation functions, these are unreliable since the analysis method is unsuitable for the wide particle size distributions obtained for the NPL.

**TEM.** TEM samples of PET NPL from glycolysis were prepared by suspending the dried NPL powder in nano-pure water. The solution was then deposited on a carbon-coated TEM grid, and filter paper was used to wick away the excess water. The samples were stained with Uranyl acetate (Uranyless 22409) for 1 min before wicking away the excess stain. Imaging was performed on a Zeiss Libra200 with an electron voltage of 110 eV and a FE gun with an accelerating voltage of 200 kV. Electron diffraction was performed with a beam stop and a 20  $\mu$ m aperture condenser.

### Statistics

All experiments were performed in triplicate to reproduce the experimental results. Error bars in figures are the standard deviation of at least 3 measurements, except for tensile testing results where averages and standard deviations are taken from at least 5 measurements.

### Data availability

The data that supports the findings of this study are available within the paper and its supplementary information. Source data for main text figures is available in the Source Data File. All data are available

from the corresponding author upon request. Source data are provided with this paper.

### References

1. Geyer, R., Jambeck, J. R. & Law, K. L. Production, use, and fate of all plastics ever made. *Sci Adv* **3**, 10.1126/sciadv.1700782 (2017).
2. Coates, G. W. & Getzler, Y. D. Y. L. Chemical recycling to monomer for an ideal, circular polymer economy. *Nat. Rev. Mater.* **5**, 501–516 (2020).
3. Frias, J. P. G. L. & Nash, R. Microplastics: Finding a consensus on the definition. *Mar. Pollut. Bull.* **138**, 145–147 (2019).
4. Nava, V., Frezzotti, M. L. & Leoni, B. Raman Spectroscopy for the Analysis of Microplastics in Aquatic Systems. *Appl. Spectrosc.* **75**, 1341–1357 (2021).
5. Morgado, V., Gomes, L., Bettencourt da Silva, R. J. N. & Palma, C. Validated spreadsheet for the identification of PE, PET, PP and PS microplastics by micro-ATR-FTIR spectra with known uncertainty. *Talanta* **234**, 122624 (2021).
6. Villacorta, A. et al. A new source of representative secondary PET nanoplastics. Obtention, characterization, and hazard evaluation. *J. Hazard Mater.* **439**, 129593 (2022).
7. Atugoda, T. et al. Nanoplastic occurrence, transformation and toxicity: a review. *Environ. Chem. Lett.* **21**, 363–381 (2023).
8. Ter Halle, A. et al. Nanoplastic in the North Atlantic Subtropical Gyre. *Environ. Sci. Technol.* **51**, 13689–13697 (2017).
9. Ivleva, N. P. Chemical analysis of microplastics and nanoplastics: challenges, advanced methods, and perspectives. *Chem. Rev.* **121**, 11886–11936 (2021).
10. C. ten Have, I. et al. Photoinduced force microscopy as an efficient method towards the detection of nanoplastics. *Chem.–Methods* **1**, 205–209 (2021).
11. Caldwell, J. et al. The micro-, submicron-, and nanoplastic hunt: A review of detection methods for plastic particles. *Chemosphere* **293**, 133514 (2022).
12. Gonçalves, J. M. & Bebianno, M. J. Nanoplastics impact on marine biota: A review. *Environ. Pollut.* **273**, 116426 (2021).
13. Azeem, I. et al. Microplastic and nanoplastic interactions with plant species: trends, meta-analysis, and perspectives. *Environ. Sci. Technol. Lett.* **9**, 482–492 (2022).
14. Roy, T., Dey, T. K. & Jamal, M. Microplastic/nanoplastic toxicity in plants: an imminent concern. *Environ. Monit. Assess.* **195**, 27 (2023).
15. Lin, S. et al. Metabolomics reveal nanoplastic-induced mitochondrial damage in human liver and lung cells. *Environ. Sci. Technol.* **56**, 12483–12493 (2022).
16. Yee, M. S.-L. et al. Impact of microplastics and nanoplastics on human health. *Nanomaterials* **11**, 496 (2021).
17. Lai, H., Liu, X. & Qu, M. Nanoplastics and Human Health: Hazard Identification and Biointerface. *Nanomaterials* **12**, 1298 (2022).
18. Microplastics are everywhere — we need to understand how they affect human health. *Nat. Med.* **30**, 913 (2024).
19. Marfella, R. et al. Microplastics and nanoplastics in atheromas and cardiovascular Events. *N. Engl. J. Med.* **390**, 900–910 (2024).
20. Pfohl, P. et al. Environmental degradation of microplastics: how to measure fragmentation rates to secondary micro- and nanoplastic fragments and dissociation into dissolved organics. *Environ. Sci. Technol.* **56**, 11323–11334 (2022).
21. Klein, S., Dimzon, I. K., Eubeler, J. & Knepper, T. P. Analysis, Occurrence, and Degradation of Microplastics in the Aqueous Environment. in *Handbook of Environmental Chemistry* vol. 58 51–67 (Springer Verlag, 2018).
22. Gewert, B., Plassmann, M. M. & MacLeod, M. Pathways for degradation of plastic polymers floating in the marine environment. *Environ. Sci. Process Impacts* **17**, 1513–1521 (2015).
23. Arhant, M., Le Gall, M., Le Gac, P.-Y. & Davies, P. Impact of hydrolytic degradation on mechanical properties of PET - Towards an

- understanding of microplastics formation. *Polym. Degrad. Stab.* **161**, 175–182 (2019).
24. Menzel, T. et al. Degradation of low-density polyethylene to nano-plastic particles by accelerated weathering. *Sci. Total Environ.* **826**, 154035 (2022).
  25. Nakatani, H., Ohshima, Y., Uchiyama, T. & Motokucho, S. Degradation and fragmentation behavior of polypropylene and polystyrene in water. *Sci. Rep.* **12**, 18501 (2022).
  26. Keith, H. D. & Padden, F. J. Spherulitic crystallization from the melt. I. Fractionation and impurity segregation and their influence on crystalline morphology. *J. Appl Phys.* **35**, 1270–1285 (1964).
  27. Yoon, D. Y. & Flory, P. J. Molecular morphology in semicrystalline polymers. *Faraday Discuss Chem. Soc.* **68**, 288 (1979).
  28. Gedde, U. W. & Hedenqvist, M. S. Morphology of Semicrystalline Polymers. in *Fundamental Polymer Science* 251–326 (Syracuse Univ Press, 2019). [https://doi.org/10.1007/978-3-030-29794-7\\_7](https://doi.org/10.1007/978-3-030-29794-7_7).
  29. Sang, T., Wallis, C. J., Hill, G. & Britovsek, G. J. P. Polyethylene terephthalate degradation under natural and accelerated weathering conditions. *Eur. Polym. J.* **136**, 109873 (2020).
  30. Lambert, S. & Wagner, M. Formation of microscopic particles during the degradation of different polymers. *Chemosphere* **161**, 510–517 (2016).
  31. Hakkarainen, M. & Albertsson, A.-C. Environmental Degradation of Polyethylene. in *Advances in Polymer Science* vol. 169 177–200 (Springer, Berlin, Heidelberg, 2004).
  32. Julinová, M. et al. Comprehensive biodegradation analysis of chemically modified poly(3-hydroxybutyrate) materials with different crystal structures. *Biomacromolecules* **24**, 4939–4957 (2023).
  33. Craig, I. H., White, J. R. & Kin, P. C. Crystallization and chemi-crystallization of recycled photo-degraded polypropylene. *Polym. (Guildf.)* **46**, 505–512 (2005).
  34. Deshoullles, Q. et al. Hydrolytic degradation of biodegradable poly(butylene adipate-co-terephthalate) (PBAT) - Towards an understanding of microplastics fragmentation. *Polym. Degrad. Stab.* **205**, 110122 (2022).
  35. Arhant, M., Gall, M. L. & Gac, P.-Y. L. Non-Arrhenian hydrolysis of polyethylene terephthalate – A 5-year long aging study above and below the glass transition temperature. *Polym. Degrad. Stab.* **215**, 110439 (2023).
  36. Ügdüler, S. et al. Towards closed-loop recycling of multilayer and coloured PET plastic waste by alkaline hydrolysis. *Green. Chem.* **22**, 5376–5394 (2020).
  37. Rubio Arias, J. J. & Thielemans, W. Instantaneous hydrolysis of PET bottles: an efficient pathway for the chemical recycling of condensation polymers. *Green. Chem.* **23**, 9945–9956 (2021).
  38. Han, M. Depolymerization of PET Bottle via Methanolysis and Hydrolysis. in *Recycling of Polyethylene Terephthalate Bottles* 85–108 (Elsevier, 2019). <https://doi.org/10.1016/B978-0-12-811361-5.00005-5>.
  39. Stanica-Ezeanu, D. & Matei, D. Natural depolymerization of waste poly(ethylene terephthalate) by neutral hydrolysis in marine water. *Sci. Rep.* **11**, 4431 (2021).
  40. Liu, P. et al. New Insights into the Aging Behavior of Microplastics Accelerated by Advanced Oxidation Processes. *Environ. Sci. Technol.* **53**, 3579–3588 (2019).
  41. Liu, P. et al. Review of the artificially-accelerated aging technology and ecological risk of microplastics. *Sci. Total Environ.* **768**, 144969 (2021).
  42. Ioakeimidis, C. et al. The degradation potential of PET bottles in the marine environment: An ATR-FTIR based approach. *Sci. Rep.* **6**, 23501 (2016).
  43. Sheel, A. & Pant, D. Chemical Depolymerization of PET Bottles via Glycolysis. in *Recycling of Polyethylene Terephthalate Bottles* 61–84 (Elsevier, 2019). <https://doi.org/10.1016/B978-0-12-811361-5.00004-3>.
  44. Shirazimoghaddam, S., Amin, I., Faria Albanese, J. A. & Shiju, N. R. Chemical Recycling of Used PET by Glycolysis Using Niobia-Based Catalysts. *ACS Eng. Au* **3**, 37–44 (2023).
  45. Luna, E. et al. Towards a better understanding of the cosolvent effect on the low-temperature glycolysis of Polyethylene Terephthalate (PET). *Chem. Eng. J.* **482**, 148861 (2024).
  46. Azimi, M. & Asselin, E. Improving surface functionality, hydrophilicity, and interfacial adhesion properties of high-density polyethylene with activated peroxides. *ACS Appl Mater. Interfaces* **14**, 3601–3609 (2022).
  47. Joshi, R., Friedrich, J., Wagner, M. & Role of Hydrogen Peroxide in Selective OH Group. Functionalization of Polypropylene Surfaces using Underwater Capillary Discharge. *J. Adhes. Sci. Technol.* **25**, 283–305 (2011).
  48. Minisci, F., Citterio, A. & Giordano, C. Electron-transfer processes: peroxydisulfate, a useful and versatile reagent in organic chemistry. *Acc. Chem. Res* **16**, 27–32 (1983).
  49. Dubelley, F. et al. Water Vapor sorption properties of polyethylene terephthalate over a wide range of humidity and temperature. *J. Phys. Chem. B* **121**, 1953–1962 (2017).
  50. Burgess, S. K. et al. Water sorption in poly(ethylene furanoate) compared to poly(ethylene terephthalate). Part 1: Equilibrium sorption. *Polym. (Guildf.)* **55**, 6861–6869 (2014).
  51. Arhant, M., Gall, M., Le & Gac, P.-Y. Le Fracture test to accelerate the prediction of polymer embrittlement during aging – Case of PET hydrolysis. *Polym. Degrad. Stab.* **196**, 109848 (2022).
  52. Fayolle, B., Audouin, L. & Verdu, J. Oxidation induced embrittlement in polypropylene — a tensile testing study. *Polym. Degrad. Stab.* **70**, 333–340 (2000).
  53. Huang, Y. & Brown, N. Dependence of slow crack growth in polyethylene on butyl branch density: Morphology and theory. *J. Polym. Sci. B Polym. Phys.* **29**, 129–137 (1991).
  54. Seguela, R. Critical review of the molecular topology of semi-crystalline polymers: The origin and assessment of intercrystalline tie molecules and chain entanglements. *J. Polym. Sci. B Polym. Phys.* **43**, 1729–1748 (2005).
  55. Keith, H. D., Padden, F. J. & Vadimsky, R. G. Intercrystalline links in polyethylene crystallized from the melt. *J. Polym. Sci. Part A-2: Polym. Phys.* **4**, 267–281 (1966).
  56. Bárány, T., Czigány, T. & Karger-Kocsis, J. Application of the essential work of fracture (EWF) concept for polymers, related blends and composites: A review. *Prog. Polym. Sci.* **35**, 1257–1287 (2010).
  57. Fayolle, B., Richaud, E., Colin, X. & Verdu, J. Review: degradation-induced embrittlement in semi-crystalline polymers having their amorphous phase in rubbery state. *J. Mater. Sci.* **43**, 6999–7012 (2008).
  58. Schultz, J. M. Microstructural aspects of failure in semicrystalline polymers. *Polym. Eng. Sci.* **24**, 770–785 (1984).
  59. Guttman, C. M., DiMarzio, E. A. & Hoffman, J. D. Modelling the amorphous phase and the fold surface of a semicrystalline polymer — the Gambler’s Ruin method. *Polym. (Guildf.)* **22**, 1466–1479 (1981).
  60. Hiejima, Y., Kida, T., Takeda, K., Igarashi, T. & Nitta, K. Microscopic structural changes during photodegradation of low-density polyethylene detected by Raman spectroscopy. *Polym. Degrad. Stab.* **150**, 67–72 (2018).
  61. Fayolle, B. & Verdu, J. Radiation aging and chemi-crystallization processes in polyoxymethylene. *Eur. Polym. J.* **47**, 2145–2151 (2011).
  62. Watson-Sanders, S. & Dadmun, M. More Efficient Chemical Recycling of Poly (Ethylene Terephthalate) by Intercepting Intermediates. *ChemSusChem* **17**, (2024).
  63. Gigault, J. et al. Nanoplastics are neither microplastics nor engineered nanoparticles. *Nat. Nanotechnol.* **16**, 501–507 (2021).

64. Kolmogorov, A. N. Über das logarithmisch normale Verteilungsgesetz der Dimensionen der Teilchen bei Zerstückelung. *Dokl. Akad. Nauk* **31**, 99–101 (1941).
65. Elazzouzi-Hafraoui, S. et al. The Shape and Size Distribution of Crystalline Nanoparticles Prepared by Acid Hydrolysis of Native Cellulose. *Biomacromolecules* **9**, 57–65 (2008).
66. Wang, Z., Schaller, M., Petzold, A., Saalwächter, K. & Thurn-Albrecht, T. How entanglements determine the morphology of semicrystalline polymers. *Proc. Natl. Acad. Sci. USA* **120**, (2023).
67. Jehanno, C. et al. Organocatalysed depolymerisation of PET in a fully sustainable cycle using thermally stable protic ionic salt. *Green. Chem.* **20**, 1205–1212 (2018).
68. Ronkay, F. et al. Melting temperature versus crystallinity: new way for identification and analysis of multiple endotherms of poly(ethylene terephthalate). *J. Polym. Res.* **27**, 372 (2020).
69. Mehta, A., Gaur, U. & Wunderlich, B. Equilibrium melting parameters of poly(ethylene terephthalate). *J. Polym. Sci.: Polym. Phys. Ed.* **16**, 289–296 (1978).
70. Cuthbertson, A. A. et al. Characterization of polymer properties and identification of additives in commercially available research plastics. *Green. Chem.* **26**, 7067–7090 (2024).
71. Cowie, J. M. G. Glass transition temperatures of stereoblock, isotactic and atactic polypropylenes of various chain lengths. *Eur. Polym. J.* **9**, 1041–1049 (1973).
72. Rieger, J. The glass transition temperature of polystyrene. *J. Therm. Anal.* **46**, 965–972 (1996).

## Acknowledgements

The authors thank Fatima Begum and Dahlia Zimmel for their help with early PET hydrolysis experiments. The authors thank Aihika Mandal and Spruha Prabhanjan Sarnaik for their help with the PP and PS degradation experiments. VS and GK thank the National Centre for Photovoltaic Research and Education (NCPRE) for using the FESEM facility. VS and GK thank the Department of Chemical Engineering for using the Dynamic light scattering facility. The authors acknowledge the use of facilities and instrumentation supported by NSF through the Columbia University, Columbia Nano Initiative, and the Materials Research Science and Engineering Center DMR-2011738. NFM, MV, SA, VP and SKK gratefully thank the National Science Foundation (Division of Materials Research, DMR-2301348) for funding. NFM acknowledges funding from the NSF GRFP through grant DGE-2036197. VS is thankful to MHRD for providing the fellowship to carry out the research. AJM acknowledges funding of the Basque Government through grant IT1503-22. MDD and SW thank the National Science Foundation (DMR) for funding.

## Author contributions

N.F.M. performed PET hydrolysis experiments and characterization, and compiled, wrote, and edited the manuscript. V.S. performed oxidative degradation and characterization of PP and PS and edited the

manuscript. M.V. supplied the theory, and IDF analysis of SAXS data, and wrote and edited the manuscript. V.P. performed sample preparation and creation for PET hydrolysis. J.K.L. performed tensile testing of PET samples. A.J.M. and L.S. aided in the discussion and editing of the manuscript. S.W. and M.D. completed the PET glycolysis experiments and characterization, as well as edited the manuscript. G.K. and S.K.K. conceived the project and wrote and edited the manuscript. All authors approve the final version of the manuscript.

## Competing interests

The authors declare no competing interests.

## Additional information

**Supplementary information** The online version contains supplementary material available at <https://doi.org/10.1038/s41467-025-58233-3>.

**Correspondence** and requests for materials should be addressed to Guruswamy Kumaraswamy or Sanat K. Kumar.

**Peer review information** *Nature Communications* thanks Yingjing Nie, Holger Ruckdaschel and the other, anonymous, reviewer(s) for their contribution to the peer review of this work. A peer review file is available.

**Reprints and permissions information** is available at <http://www.nature.com/reprints>

**Publisher's note** Springer Nature remains neutral with regard to jurisdictional claims in published maps and institutional affiliations.

**Open Access** This article is licensed under a Creative Commons Attribution-NonCommercial-NoDerivatives 4.0 International License, which permits any non-commercial use, sharing, distribution and reproduction in any medium or format, as long as you give appropriate credit to the original author(s) and the source, provide a link to the Creative Commons licence, and indicate if you modified the licensed material. You do not have permission under this licence to share adapted material derived from this article or parts of it. The images or other third party material in this article are included in the article's Creative Commons licence, unless indicated otherwise in a credit line to the material. If material is not included in the article's Creative Commons licence and your intended use is not permitted by statutory regulation or exceeds the permitted use, you will need to obtain permission directly from the copyright holder. To view a copy of this licence, visit <http://creativecommons.org/licenses/by-nc-nd/4.0/>.

© The Author(s) 2025